Geochemical Perspectives Letters

A two-stage impact melting process in an impact glass strewn field from the Atacama Desert

P. Rochette, G. Di Vincenzo, J. Gattacceca, J.A. Barrat, B. Devouard, L. Folco, A. Musolino, Y. Quesnel

Supplementary Information

The Supplementary Information includes:

- Samples and Methods
- Estimating Extraterrestrial Contamination
- Mixture of the Silica-rich and Normal Glasses?
- Tables S-1 to S-5
- Figures S-1 to S-10
- Supplementary Information References

Samples and Methods

Magnetic susceptibility of all silica-rich glass was measured using a MFK1 bridge (Rochette *et al*., 2015). For detailed analysis, three samples were selected from the western strewn-field, two from El Medano (EM1a and EM2b) and one from Caleta el Cobre (CeC) meteorite collection areas (Hutzler *et al*., 2016), distant by 25 km (Fig. 1). Systematic investigation of samples from the main strewn-field revealed also translucent teardrop samples and three of them from different sites were included in the analytical batch. Macroscopic examples of silica-rich and normal samples are presented in Figures S-1 and S-7, respectively.

These six samples were analysed for major and trace elements by ICP-AES, ICP-OES and ICP-MS in SARM Nancy and UBO Brest. They were compared to 12 analyses reported in Gattacceca *et al*. (2021) on normal atacamaites. Isotopic ratio for Sr and Nd were determined in SARM Nancy and UBO Brest. In SARM, major element compositions were measured using an emission spectrometer ICP-OES (ICap 6500 Thermo Fischer), and trace elements by ICP-MS (Thermo Elemental X7) following the method detailed in Carignan *et al*. (2001). Typical analytical precisions were ca. 2 % for major elements and 5–8 % for trace elements. In UBO 100–150 mg of atacamaites were digested on a hot plate heated to 125 °C, using sequential mixtures of HF/HNO_3, HNO_3 and HCl. The aliquots of the obtained solutions were used for the determination of major and trace element concentrations, Sr and Nd isotopic compositions. Major elements, Ni and Co abundances were analysed by inductively coupled plasma-atomic emission spectrometry (ICP-AES) using a Horiba Jobin Yvon Ultima spectrometer and following the analytical procedure of Cotten *et al*. (1995). Relative standard deviations are <2 %. The accuracy is better than 7 % for Na and P, and much better than 3 % for the other elements. Trace element concentrations were measured with a Thermo® Element2 ICP-SFMS (inductively coupled plasma-sector field mass spectrometer). Concentrations were determined following the procedure described by Barrat *et al*. (2012, 2016). Based on results obtained on many standards, the reproducibility and accuracy are always better than 5 %. Strontium and Nd fractions were prepared following conventional ion exchange techniques. They were analysed using a Thermo® Triton TIMS (thermal ionisation mass spectrometer). Isotopic ratios were normalised against $^{86}Sr/^{88}Sr = 0.1194$ and $^{146}Nd/^{144}Nd = 0.7219$. The values obtained for NBS 987 and La Jolla standards during the course of the study are respectively $^{87}Sr/^{86}Sr = 0.710254 \pm 0.000003$ (2σ, $n = 8$) and $^{143}Nd/^{144}Nd = 0.511830 \pm 0.000003$ (2σ, $n = 6$).

Microscopic observations were performed using Hitachi S3000-N instrument scanning electronic microscope (SEM) in backscattered mode operated at 15 kV, equipped with a Bruker energy dispersive spectrometry (EDS) microanalysis system. Microanalyses were obtained by electron microprobe analysis using a CAMECA SX-100 at the Centre de Microanalyse de Paris VI (CAMPARIS). The operating conditions were 15 kV accelerating voltage with a current of 15 nA and a defocused beam of 10 µm. Both natural and synthetic standards were used for calibration: albite for Na; anorthite for Al; apatite for P; wollastonite for Si, Ca; orthoclase for K; pyrite for S; $MnTiO_3$ for Mn and Ti; fayalite for Fe; forsterite for Mg, and NiO for Ni. The detection limits were 723 µg g^{-1} for K, 684 µg g^{-1} for Ca, 499 µg g^{-1} for Al, 959 µg g^{-1} for Na, 639 µg g^{-1} for Si, 544 µg g^{-1} for Mg, 494 µg g^{-1} for P, 767 µg g^{-1} for Mn, 384 µg g^{-1} for Ni, 797 µg g^{-1} for Fe, and 795 µg g^{-1} for Ti.

$^{40}Ar/^{39}Ar$ analyses were performed at IGG–CNR (Pisa, Italy) on three samples from the normal glass (samples K51, K48G, K326) and one sample (EM1a) from the silica-rich type. Glass samples were crushed and sieved, and glass separates were recovered from the 0.35–0.50 mm grain size. $^{40}Ar/^{39}Ar$ analyses were performed using both the laser step-heating and the laser total fusion techniques. Glass separates, after final cleaning by alternating methanol and deionised water, were wrapped in Al foil and irradiated along with the Alder Creek sanidine (ACs) in the core of the TRIGA reactor at the Università di Pavia (Italy) in three distinct batches for three hours (Table S-3): 1) irradiation PAV-87, May 2021; 2) irradiation PAV-88, March 2022; 3) irradiation PAV-89, October 2022. Argon isotope compositions were determined using either a single-collector noble gas mass spectrometer (irradiation PAV-88 and only step-heating analysis) or a multi-collector mass spectrometer (irradiation PAV-87 and PAV-88). The neutron fluence was monitored by analysing single grains of the ACs, which were melted using a continuous wave CO_2 laser (New Wave Research MIR10– 30 CO_2 laser system). Laser step-heating and total fusion experiments of glass separates were performed using either (see Table S-3) a fiber laser (RedEnergy G4 50W EP-Z, SPI Lasers, 1059–1065 nm) or the same CO_2 laser as above. The laser beams were defocused to 2-mm spot size and slowly rastered over the glass separate. Steps were carried out at increasing laser power until complete melting. Argon isotope compositions determined through the single-collector noble gas mass spectrometry were acquired by peak jumping using a MAP215-50 (Mass Analyser Products) mass spectrometer, fitted with a secondary electron multiplier. Gas purification (10 min, including ~2 min of lasering) was achieved by one SAES C-50 getter held at 400 °C and one Saes CapaciTorr HV200 getter held at room temperature. Blanks were analysed every three to four analyses. A polynomial function was fit to blanks analysed during the day of acquisition, and unknown analyses were corrected based on the time of measurement. Line blank variation is given in the Table S-3. More details about mass spectrometer analysis can be found in Di Vincenzo and Skála (2009). Argon isotope compositions determined through the multi-collector noble gas mass spectrometry were acquired simultaneously using an ARGUS VI (Thermo Fisher Scientific) mass spectrometer. Ar isotopes from 40 to 37 were acquired using Faraday detectors, equipped with 10^{12} Ω resistors for ^{40}Ar and 10^{13} Ω resistors for ^{39}Ar, ^{38}Ar and ^{37}Ar. Faraday detectors were cross calibrated for the slight offset using air shots. Before the acquisition of data from irradiation PAV-88, the mass spectrometer was upgraded with an additional amplifier equipped with a 10^{13} Ω resistor on cup H1 (^{40}Ar). ^{36}Ar was measured using a Compact Discrete Dynode (CDD) detector. Gas purification (4 min, including ~1 min of lasering) was achieved using three SAES NP10 getters (one water cooled, held at ~400 C and two at room temperature). Blanks were generally monitored every two runs and were subtracted from succeeding sample results. Line blanks are given in the Table S-2. More details about mass spectrometer calibration and analysis can be found in Di Vincenzo *et al*. (2021). The correction factors for interfering isotopes from K and Ca were determined on K-rich and Ca-rich glasses and are listed in Table S-3. Ages were calculated using decay constants recalculated by Min *et al*. (2000), an atmospheric $^{40}Ar/^{36}Ar$ ratio of 298.56 ± 0.31 (Lee *et al*., 2006), and an age of 1.1848 ± 0.0012 Ma for the ACs reference mineral (Niespolo *et al*., 2017). Data corrected for post-irradiation decay, mass discrimination effects and blanks (relative abundances) are listed in Table S-3. Uncertainties on single runs are 2σ analytical uncertainties, including in-run statistics and uncertainties in the discrimination factor, interference corrections and procedural blanks. Uncertainties on the total gas ages and on error-weighted means also include the uncertainty on the fluence monitor (2σ internal errors). The full uncertainty given for the mean age from normal glass also include systematic uncertainties (on the age of the reference material and on ^{40}K total decay constant). Repeated analyses of individual fragments of moldavite VLTA2242 (Di Vincenzo, 2022) were used for accuracy control of the acquired $^{40}Ar/^{39}Ar$ data. Data relative to irradiation PAV-87 are reported in Di Vincenzo (2022), those relative to irradiations PAV-88 and PAV-89 are listed in Table S-3. Data for three different stack positions from irradiation PAV-88 and PAV-89 yielded a pooled mean age of 14.7520 ± 0.0098 Ma (Table S-3), which is indistinguishable at 1σ level from the value (14.7495 ± 0.0045 Ma) reported in Di Vincenzo (2022). The mean age of 6.578 ± 0.011 Ma (±0.013 Ma including all sources of errors) reported in the main text for the

normal glass has been calculated using the pooled R-value (Atacamaite/ACs) of 5.560 ± 0.010 (± 2σ, MSWD = 0.63, Probability 0.75), derived from intra-sample concordant $^{40}Ar/^{39}Ar$ data from step-heating and total fusion data, and using equations and error propagation given in Renne *et al*. (1998). The R-value provides a useful means for allowing a direct comparison of a reference material and an unknown sample regardless of the assumed age (see Karner and Renne, 1998), and consists of the ratio between the $^{40}Ar^*/^{39}Ar_K$ ratios of two co-irradiated samples. The R-value reported here can be therefore used in the future to update the age of the atacamaites whenever the age of the ACs reference material is refined.

Estimating Extraterrestrial Contamination

In Gattacceca *et al*. (2021), the Co and Ni *versus* Fe correlations shown by normal atacamaites were used to estimate a metallic impactor composition with Ni and Co contents of 5.4 and 0.45 wt. %, respectively. We provide in Figure S-8 a mixing curve between this model impactor and a model rock containing 19.2 ppm Ni and 10 ppm Co. This model composition was derived from the average Ni content of the model andesite derived from Oliveros *et al*. (2020) and the Co content providing the best fit for the Si-rich glass.

The model confirms that normal atacamaites except one sample (PT7e, see discussion below) show contamination varying from 3 to 9 %. On the other hand, it points toward a 0.1 to 0.2 % of contamination for the silica-rich samples. However, this estimate is an upper bound as there is a strong possibility of enrichment in the silica-rich target material by Ni and Co unrelated to the impactor. It could be due to accumulation of micrometeorites on the surface. Indeed, the surface of the Atacama Desert is a good accumulator for micrometeorites due to its very old age (van Ginneken *et al*., 2017). Moreover, the heavy mineral enrichment invoked for explaining the enrichment in *e.g.*, Ti, Cr, Zr of Figure 3b, could also have enriched the target in Ni and Co. Therefore, we can safely state that 0.1–0.2 % is the upper bound of impactor contamination in the silica-rich glass in these 6 samples. A significant contamination by an iron impactor should also be seen on the magnetic susceptibility data, which is available on 124 samples. A 2 % impactor contamination should result in a Fe_2O_3 content increasing from 4.64 to 7.5 wt. %. This would result in a strong change of susceptibility even if all iron is kept paramagnetic (77 to 128 × 10^{-9} m^3/kg). Only one out of 124 samples showed anomalously high susceptibility due to insertion of a normal atacamaite droplet. So, we can conclude that less than a percent of high silica glass may show significant impactor contamination (*i.e.* >1 %).

Mixture of the Silica-rich and Normal Glasses?

The homogeneity of chemical composition of the six silica-rich studied sample also precludes a significant mixing with normal atacamaite. Among 124 silica-rich samples, identified by their translucent character, only one had a diverging magnetic susceptibility (K260m), the others being well grouped around the mean susceptibility value. This indicates a rather constant iron amount (see Fig. S-3). Mixing in equal proportion the two melt batches (with average susceptibilities of 77 and 191 × 10^{-9} m^3/kg, respectively) would result in an increase of magnetic susceptibility of a factor 1.7 (at least, *i.e.* without ferromagnetic contribution). It should also show visually during the translucency test. Therefore, we can conclude that composite samples with significant inclusion of normal atacamaite constitute at most 1 % of the collection.

K260M sample is a unique case where we identified a millimetric droplet of magnetite-rich normal atacamaite, inserted in a hole of a silica-rich sample from the main strewn field. Such a find indicates that the two particles, present independently in the impact plume, were welded together before cooling, thus likely in flight. This apparently contradicts our two-stage scheme (Fig. S-6) with the normal atacamaite being launched after the silica-rich material. However, it is possible to invoke a combination of trajectories allowing these two particles to encounter during the descending flight of the silica-rich particle (Fig. S-9).

Now, what if full mixture of the two melts remained undetected in the normal atacamaite collection? In particular, could the weakly contaminated PT7e sample represent such a mixture (as suggested in Fig. S-8)? The chemical composition of PT7e clearly excludes this hypothesis based on the lack of alkali depletion, typical of silica-rich material (compare Fig. S-10 and Fig. 3b). The fit between PT7e and normal atacamaite, apart on Ni and Co, clearly point toward PT7e being fully derived from the same target material but with a much lower extra-terrestrial contamination (about 0.7 %).

Supplementary Tables

Table S-1 Results of electron probe microanalyses (EPMA) for 5 transparent atacamaites (in wt. %) and the composite sample K260M (Fig. S-1d).

Sample	SiO_2	Al_2O_3	TiO_2	FeO	MnO	MgO	CaO	Na_2O	K_2O	NiO	total
K260-46	87.16	0.45	7.23	3.82	bdl	1.13	0.15	bdl	0.28	bdl	100.34
	86.67	0.57	7.40	3.89	bdl	0.98	0.16	bdl	0.29	bdl	100.07
	85.85	0.51	7.92	4.04	bdl	0.79	0.10	bdl	0.31	bdl	99.61
	87.44	0.46	7.53	3.82	bdl	0.82	0.19	bdl	0.30	bdl	100.67
K260-49	85.60	0.64	8.19	4.40	0.09	0.68	0.11	bdl	0.33	bdl	100.11
	85.45	0.58	8.69	4.16	0.10	0.70	0.10	bdl	0.30	bdl	100.16
	85.63	0.50	8.58	4.21	0.08	0.79	0.13	bdl	0.31	bdl	100.32
	85.31	0.60	8.39	4.05	0.10	0.82	0.00	bdl	0.34	bdl	99.66
K260-59	85.41	0.50	8.72	3.98	bdl	0.67	0.10	bdl	0.29	bdl	99.77
	85.96	0.52	8.33	4.36	bdl	0.70	0.10	bdl	0.28	bdl	100.38
	85.96	0.68	8.47	3.96	bdl	0.76	0.14	bdl	0.26	bdl	100.37
	84.92	0.61	8.57	4.28	bdl	0.73	0.07	bdl	0.24	bdl	99.53
K526-3	84.88	0.52	8.29	4.24	bdl	0.87	0.15	bdl	0.32	bdl	99.34
EM1a	85.48	0.54	8.26	4.25	0.11	0.91	0.09	bdl	0.27	bdl	99.98
mean	85.84	0.55	8.18	4.10	bdl	0.81	0.11	bdl	0.29	bdl	100.02
s.d.	0.74	0.06	0.47	0.19		0.12	0.05		0.03		0.38
Detection limit	0.06	0.05	0.08	0.08	0.08	0.05	.07	0.09	0.07	0.04	
composite sample											
K260M normal inclusion	60.13	0.37	12.17	11.18	0.06	1.28	5.11	3.04	2.75	0.53	96.65
K260M high-silica	84.84	0.71	7.99	4.05	0.06	0.77	0.10	0.05	0.25	bdl	98.85

Table S-2 Major element abundances (in wt. %) measured by ICP-OES (or ICP-MS for K301 and K272). Average value for normal atacamaites after Gattacceca *et al.* (2021). See main text and Figure 4 for model ratio. Rock composition reported from Oliveros *et al.* (2020) and selected within a two degrees square centered on the main strewn-field (24–26° S, 66.5–68.5° W). Rock 1: average of 4 analyses of the coastal batholith with SiO_2 within 61–64 wt. % and isotopic data similar to those of normal atacamaites. Rock 2: coastal batholith analysis with high SiO_2 content.

	CeC	EM1A	EM2B	K301	K527-37	K260-34	mean	s.d.	Normal atacamaite	model ratio	Rock1	Rock2
SiO_2	85.75	85.44	85.08			85.37	85.41	0.28	63.71	1.00	62.06	84.96
Al_2O_3	8.41	7.88	7.16			7.80	7.81	0.51	13.10	1.48	15.13	7.56
Fe_2O_3	4.74	4.83	4.25			4.72	4.64	0.26	9.78	1.18	6.18	1.10
MnO	0.059	0.059	0.085	0.072	0.071	0.071	0.07	0.01	0.08	2.16	0.11	0.02
MgO	0.84	0.99	1.44			1.03	1.07	0.26	1.92	1.39	2.97	0.54
CaO	0.15	0.17	0.32			0.19	0.21	0.07	4.62	0.11	5.64	0.28
Na_2O	0.04	0.06	0.05			0.05	0.05	0.01	3.56	0.03	3.83	2.45
K_2O	0.28	0.29	0.29	0.27	0.28	0.30	0.29	0.01	2.98	0.24	2.59	1.41
TiO_2	0.57	0.54	0.54	0.56	0.55	0.55	0.55	0.01	0.53	2.58	0.98	0.28
LOI	−0.76	−0.11	−0.32			0.20	−0.25	0.40				
total	100.08	100.15	98.89			100.28	99.85	0.65				

Table S-3 ^{40}Ar-^{39}Ar total fusion and step-heating data on impact glasses from the Atacama Desert (Chile) and moldavite VLTA2242 (for accuracy control).

Table S-3 is available for download (.xlsx) from the online version of this article at http://doi.org/10.7185/geochemlet.2418.

Table S-4 Trace element abundances (μg g^{-1}) determined by ICPMS. Rock composition reported from Oliveros *et al*. (2020) and selected within a two degrees square centered on the main strewn-field (24–26° S, 66.5–68.5° W). Rock 1: average of 4 analyses of the coastal batholith with SiO_2 within 61–64 wt. % and isotopic data similar to those of normal atacamaites. Rock 2: coastal batholith analysis with high SiO_2 contents.

	CeC	TEM1A	TEM2B	K301	K527-37	K260-34	mean	s.d.	Normal atacamaite	model ratio	Rock1	Rock2
Li				8.81	8.67		**8.74**	0.10	51.1	0.43		
Be	0.55	0.55	0.57	0.54	0.62	0.57	**0.57**	0.03	2.03	0.69		
Sc	9.38	8.97	8.46	9.49	9.05	8.94	**9.05**	0.37	9.76	2.31	17	<5
V	43.89	51.96	32.52	52.70	55.40	54.74	**48.54**	8.87	83.3	1.45	147	14
Cr	96.51	126.75	92.53	98.05	101.79	134.79	**108.40**	17.76	30.5	8.84	45.7	16
Co	14.51	17.26	15.91	16.67	15.93	18.30	**16.43**	1.30	217	0.19		
Ni	79.08	121.29	75.52	98.29	97.23	131.62	**100.50**	22.36	2556	0.10	19.3	<10
Rb	14.73	15.41	14.92	15.84	15.65	15.78	**15.39**	0.47	96.4	0.40	122	47.2
Sr	24.35	26.84	31.08	37.99	34.05	60.51	**35.80**	13.05	231.3	0.38	235	61
Y	16.23	15.90	15.85	19.03	18.74	16.24	**17.00**	1.47	39	1.08	31.7	20
Zr	203.40	197.06	214.94	224.49	220.77	203.85	**210.75**	10.92	179.7	2.92	368	269
Nb	8.75	8.58	8.60	10.38	10.17	8.80	**9.22**	0.83	11.2	2.05	10.25	7
Cs	2.61	2.77	2.38	1.51	1.66	2.80	**2.29**	0.57	5.7	1.00	5.44	0.87
Ba	162.47	160.41	218.98	209.81	196.59	231.20	**196.58**	29.49	634	0.77	271	196
La	23.59	22.80	22.18	26.09	25.24	24.40	**24.05**	1.48	37.6	1.59	18.3	5.73
Ce	42.27	40.11	38.97	47.55	46.50	42.29	**42.95**	3.42	72.1	1.48	45.75	20.13
Pr	5.48	5.26	5.28	6.14	5.95	5.62	**5.62**	0.36	8.5	1.64	6.11	2.56
Nd	20.66	19.79	20.03	22.92	22.43	21.18	**21.17**	1.27	33.2	1.59	25.44	10.38
Sm	3.89	3.80	3.85	4.26	4.18	4.09	**4.01**	0.19	6.8	1.46	5.71	2.36
Eu	0.84	0.80	0.83	0.90	0.89	0.87	**0.85**	0.04	1.1	1.96	1.18	0.4
Gd	3.31	3.17	3.17	3.55	3.48	3.29	**3.33**	0.16	6.3	1.31	5.51	2.41
Tb	0.51	0.49	0.49	0.55	0.55	0.51	**0.51**	0.03	1.0	1.29	0.86	0.43
Dy	3.05	2.94	2.97	3.19	3.20	3.05	**3.07**	0.11	6.0	1.27	5.28	2.84
Ho	0.63	0.61	0.61	0.66	0.65	0.63	**0.63**	0.02	1.2	1.26	1.07	0.59
Er	1.73	1.65	1.65	1.87	1.88	1.72	**1.75**	0.10	3.6	1.21	3.08	1.67
Yb	1.77	1.73	1.68	1.91	1.88	1.75	**1.79**	0.09	3.5	1.25	2.82	1.54
Lu	0.27	0.26	0.26	0.27	0.28	0.27	**0.27**	0.01	0.55	1.21	0.42	0.21
Hf	5.46	5.28	5.59	6.06	5.97	5.44	**5.63**	0.31	5.3	2.64	9.25	8
Ta	0.81	0.78	0.78	0.74	0.76	0.81	**0.78**	0.03	0.93	2.08		
Pb	1.05	3.60	1.22	1.89	1.77	3.85	**2.23**	1.20	2.3	2.41		
Th	6.81	6.54	6.05	7.60	7.52	6.74	**6.88**	0.59	11.6	1.47	13.76	5.56
U	0.71	0.84	0.47	0.82	0.93	0.97	**0.79**	0.18	1.8	1.09	2.91	1

Table S-5 Sr and Nd isotopic data table. Uncertainties (2σ) on $^{87}Sr/^{86}Sr$ and $^{143}Nd/^{144}Nd$ ratios are 0.000006 and 0.000004, respectively. Rock 1 and 2 after Oliveros *et al*. (2020). Average for normal atacamaite (SA) after Gattacceca *et al*. (2021).

	$^{87}Sr/^{86}Sr$	εNd	$^{143}Nd/^{144}Nd$
CeC	0.719403	−9.9	0.512133
K260	0.713003	−9.7	0.512142
TEM1A	0.719189	−9.9	0.512130
TEM2B	0.717991	−9.9	0.512132
SA	0.7078	+0.1	
Rock 1	0.7079	+1.5	0.51272
Rock 2	0.7156	−9.7	0.51214

Supplementary Figures

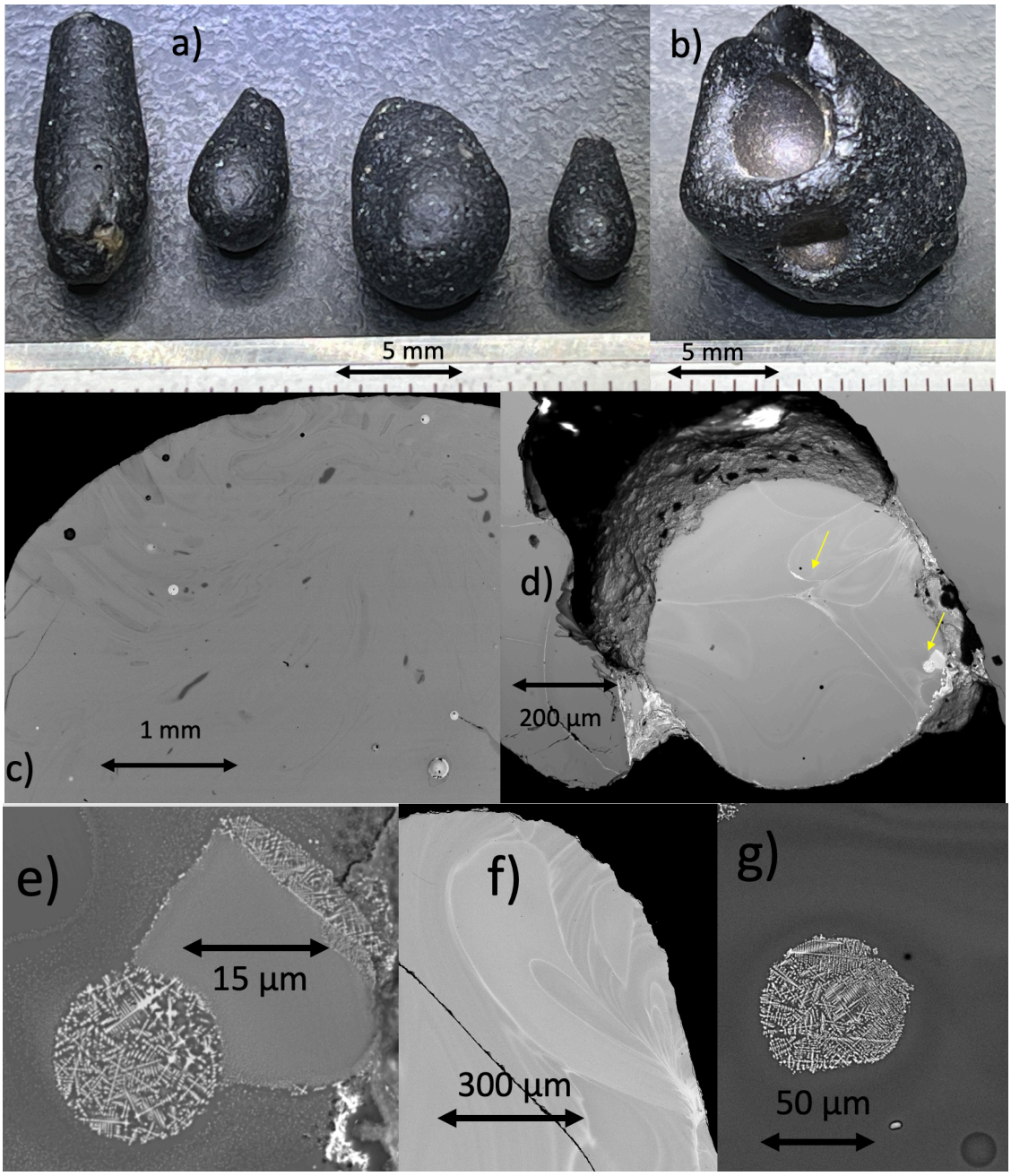

Figure S-1 Examples of full silica-rich samples with a millimetric scale: **(a)** tear drops from EM site and **(b)** largest sample from the main field (K258); backscattered SEM images of **(c)** EM1a sample (field of view is 4 mm) and **(d)** composite sample K260m. Note the average heavier element composition in the spherule enclosed within the darker silica rich sample, as well as bands rich in Fe and Ni within the spherule (left arrow). **(e)** Details of the Ni,Fe rich spherule in **(d)** (right arrow); **(f)** and **(g)** Fe- rich banding and a Fe,Ni rich spherule within normal atacamaites.

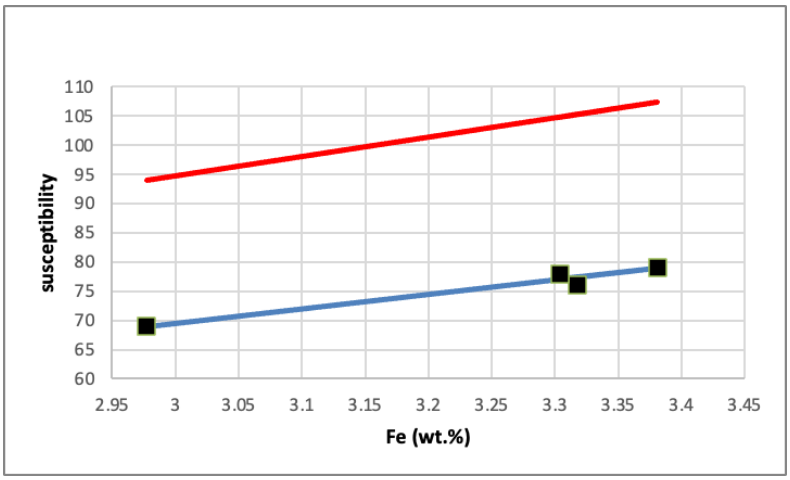

Figure S-2 Magnetic susceptibility (in 10^{-9} m^3/kg) *versus* elemental iron abundance for the analysed silica rich glasses. Data (squares) compared to modelled paramagnetic susceptibilities for Fe^{2+} (blue) and Fe^{3+} (red), after Rochette *et al.* (2015).

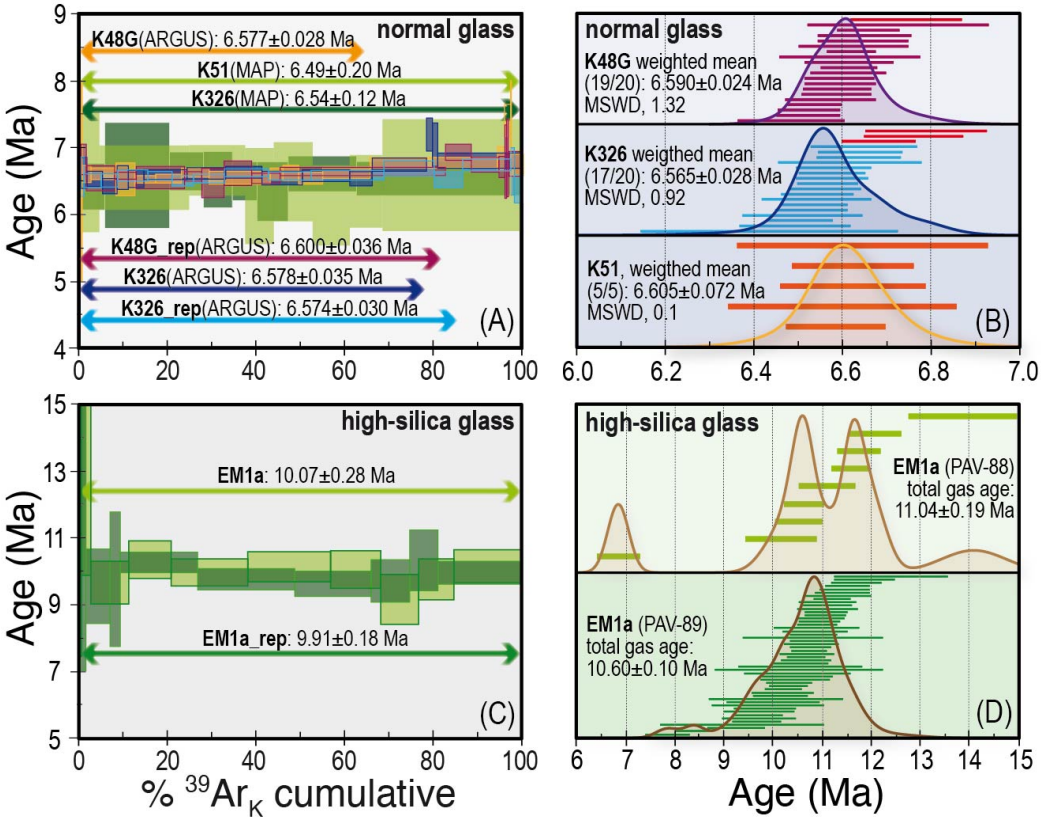

Figure S-3 **(a–c)** age spectra from step-heating experiments of normal **(a)** and high-silica glasses **(c)**. Age spectra in **(a)** affected by larger uncertainties were completed through the single-collector noble gas mass spectrometer (see Methods and Table S-3). **(b–d)** Cumulative probability and ranked distribution of $^{40}Ar/^{39}Ar$ apparent dates of normal **(b)** and high-silica **(d)** glass fragments from total fusion experiments. Data were collected from 1 to 6 fragments from the 0.35–0.50 mm grain size. Uncertainties on single runs are 2σ analytical errors. Uncertainties on the error-weighted means of total gas dates also include the uncertainty on the fluence monitor (2σ internal errors).

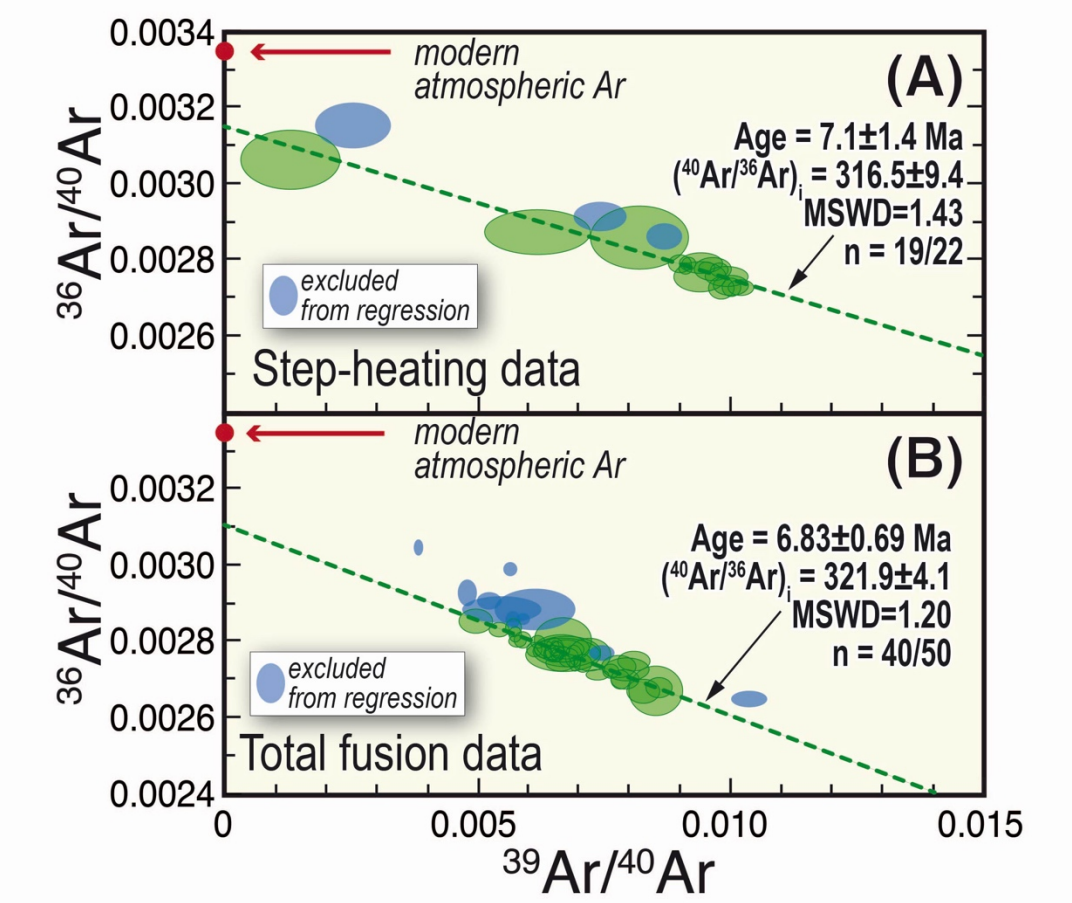

Figure S-4 Isochron plots (three-isotope correlation diagram, $^{36}Ar/^{40}Ar$ *versus* $^{39}Ar/^{40}Ar$) for **(a)** step-heating and **(b)** total fusion data of the high-silica glass sample EM1a. See main text for details. Step-heating and total fusion data define a triangular envelop that requires at least three distinct Ar components: (1) atmospheric Ar; (2) a radiogenic Ar component with dates of ~6.5–7 Ma; and (3) extraneous Ar with a $^{40}Ar/^{36}Ar$ ratio of ~320.

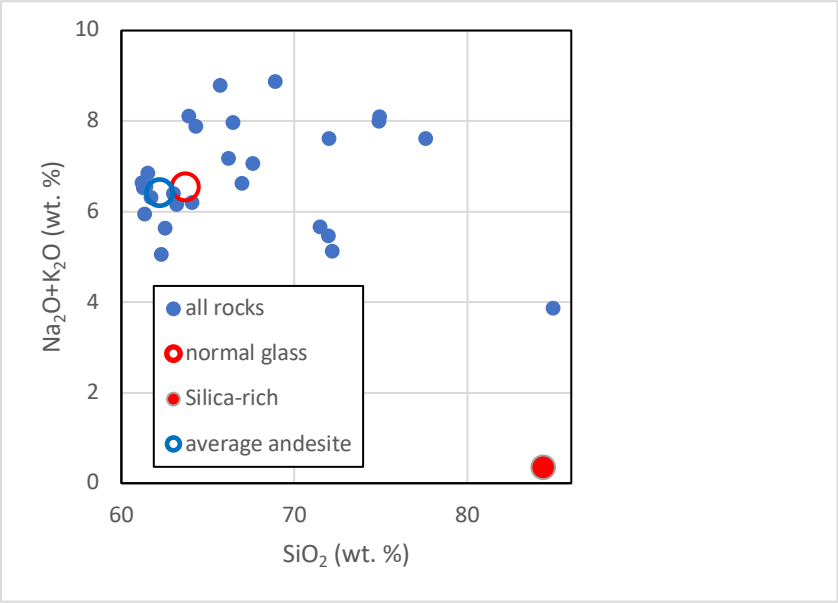

Figure S-5 TAS diagram (K_2O + Na_2O *versus* SiO_2) for average silica-rich glass (closed red circle), normal atacamaite (open red circle) and coastal batholith with SiO_2 in the 61–64 wt. % SiO_2 range and Sr, Nd isotopic ratio close to the one of normal atacamaite (data used for Fig. 3a). Small closed blue circles are all individual data from Oliveros *et al*. (2020) within a two degrees square centered on the main strewn-field (24–26° S, 66.5–68.5° W), cut above SiO_2 = 60 wt. %.

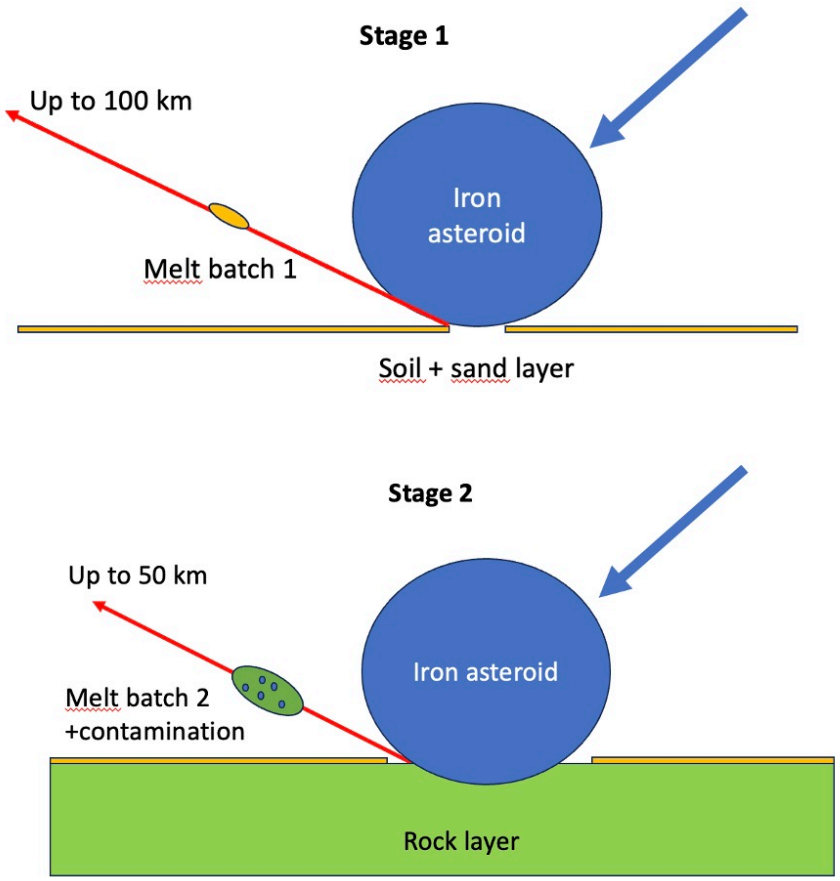

Figure S-6 Sketch of our model for two stage impact melting and ejecta.

Figure S-7 Macroscopic images of normal atacamaites: **(a)** three pieces *in situ*; **(b)** assortment of typical splash form shapes.

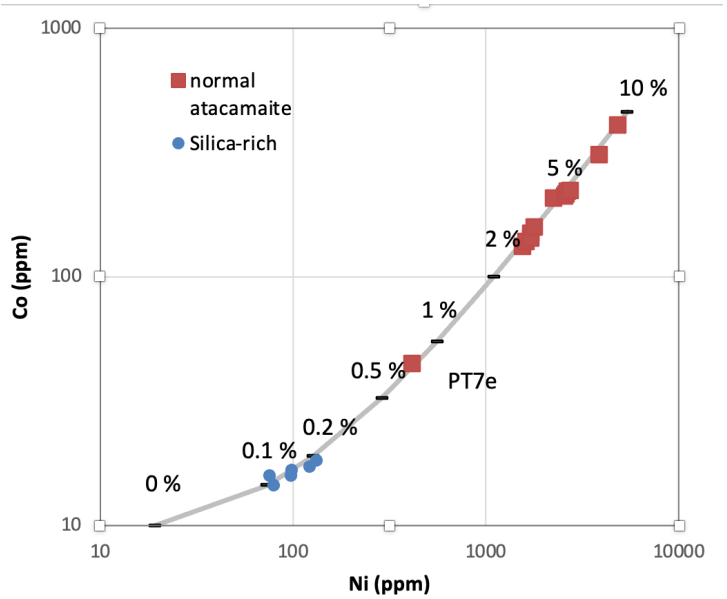

Figure S-8 Co *versus* Ni content of atacamaites superposed on a mixing model between impactor and fresh andesite.

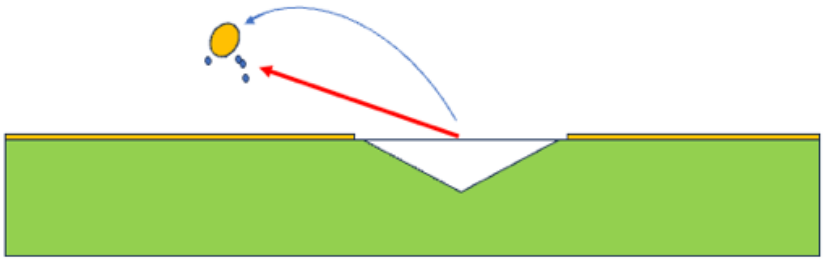

Figure S-9 Conceptual sketch explaining how K260m composite sample formed (yellow first launched silica-rich centimetric particle; blue secondary normal glass millimetric particles; based on Fig. 11 of Carlson *et al*., 2023).

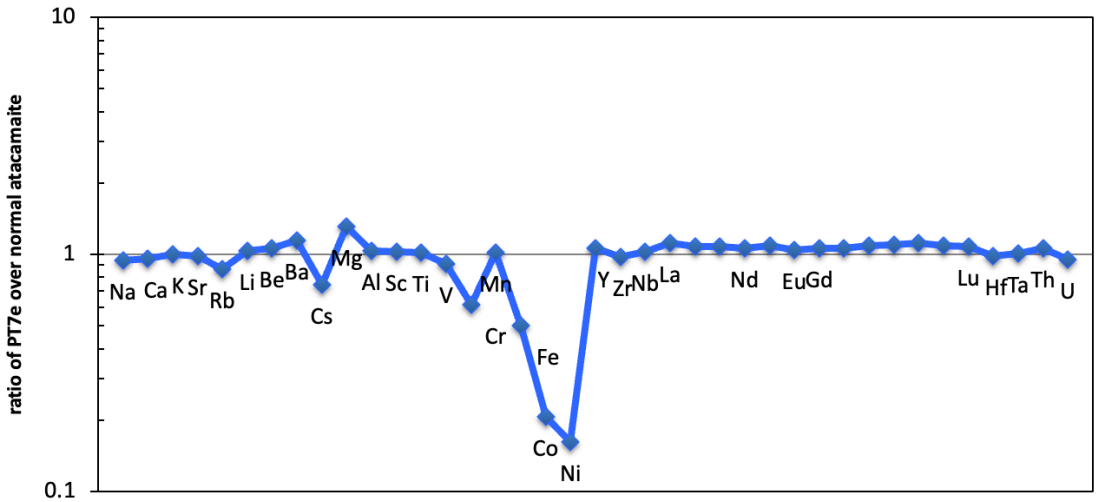

Figure S-10 Plot of PT7e sample normalised to average normal atacamaite (PT7e was not used to compute this average), following the same element ordering as Figure 3b.

Supplementary Information References

Barrat, J.A., Zanda, B., Moynier, F., Bollinger, C., Liorzou, C., Bayon, G. (2012) Geo-chemistry of CI chondrites: Major and trace elements, and Cu and Zn isotopes. *Geochimica et Cosmochimica Acta* 83, 79–92. https://doi.org/10.1016/j.gca.2011.12.011

Barrat, J.A., Dauphas, N., Gillet, P., Bollinger, C., Etoubleau, J., Bischoff, A., Yamaguchi, A. (2016) Evidence from Tm anomalies for non-CI refractory lithophile element proportions in terrestrial planets and achondrites. *Geochimica et Cosmochimica Acta* 176, 1–17. https://doi.org/10.1016/j.gca.2015.12.004

Carignan, J., Hild, P., Mevelle, G., Morel, J., Yeghicheyan, D. (2001) Routine Analyses of Trace Elements in Geological Samples using Flow Injection and Low Pressure On-Line Liquid Chromatography Coupled to ICP-MS: A Study of Geochemical Reference Materials BR, DR-N, UB-N, AN-G and GH. *Geostandards Newsletter* 25, 187–198. https://doi.org/10.1111/j.1751-908X.2001.tb00595.x

Carlson, M.A., Melosh, H.J., Johnson, B.C. (2023) Atmospheric Interactions of Ejecta on Earth and Mars Including the Effect of Vaporization. *The Planetary Science Journal* 4, 194. https://doi.org/10.3847/PSJ/acf9f1

Cotten, J., Le Dez, A., Bau, M., Caroff, M., Maury, R.C., Dulski, P., Fourcade, S., Bohn, M., Brousse, R. (1995) Origin of anomalous rare-earth element and yttrium enrichments in subaerially exposed basalts: Evidence from French Polynesia. *Chemical Geology* 119, 115–138. https://doi.org/10.1016/0009-2541(94)00102-E

Di Vincenzo, G. (2022) High precision multi-collector $^{40}Ar/^{39}Ar$ dating of moldavites (Central European tektites) reconciles geochronological and paleomagnetic data. *Chemical Geology* 608, 121026. https://doi.org/10.1016/j.chemgeo.2022.121026

Di Vincenzo, G., Skála, R. (2009) $^{40}Ar–^{39}Ar$ laser dating of tektites from the Cheb Basin (Czech Republic): Evidence for coevality with moldavites and influence of the dating standard on the age of the Ries impact. *Geochimica et Cosmochimica Acta* 73, 493–513. https://doi.org/10.1016/j.gca.2008.10.002

Di Vincenzo, G., Folco, L., Suttle, M.D., Brase, L., Harvey, R.P. (2021) Multi-collector $^{40}Ar/^{39}Ar$ dating of microtektites from Transantarctic Mountains (Antarctica): A definitive link with the Australasian tektite/microtektite strewn field. *Geochimica et Cosmochimica Acta* 298, 112–130. https://doi.org/10.1016/j.gca.2021.01.046

Gattacceca, J., Devouard, B., Barrat, J.-A., Rochette, P., Balestrieri, M.L., *et al*. (2021) A 650 km^2 Miocene strewnfield of splash-form impact glasses in the Atacama Desert, Chile. *Earth and Planetary Science Letters* 569, 117049. https://doi.org/10.1016/j.epsl.2021.117049

Hutzler, A., Gattacceca, J., Rochette, P., Braucher, R., Carro, B., Christensen, E.J., Cournede, C., Gounelle, M., Laridhi Ouazaa, N., Martinez, R., Valenzuela, M., Warner, M., Bourles, D. (2016) Description of a very dense meteorite collection area in western Atacama: Insight into the long-term composition of the meteorite flux to Earth. *Meteoritics and Planetary Science* 51, 468–482. https://doi.org/10.1111/maps.12607

Karner, D.B., Renne, P.R. (1998) $^{40}Ar/^{39}Ar$ geochronology of Roman volcanic province tephra in the Tiber River valley: Age calibration of middle Pleistocene sea-level changes. *GSA Bulletin* 110, 740–747. https://doi.org/10.1130/0016-7606(1998)110<0740:AAGORV>2.3.CO;2

Lee, J.-Y., Marti, K., Severinghaus, J.P., Kawamura, K., Yoo, H.-S., Lee, J.B., Kim, J.S. (2006) A redetermination of the isotopic abundances of atmospheric Ar. *Geochimica et Cosmochimica Acta* 70, 4507–4512. https://doi.org/10.1016/j.gca.2006.06.1563

Min, K., Mundil, R., Renne, P.R., Ludwig, K.R. (2000) A test for systematic errors in $^{40}Ar/^{39}Ar$ geochronology through comparison with U/Pb analysis of a 1.1-Ga rhyolite. *Geochimica et Cosmochimica Acta* 64, 73–98. https://doi.org/10.1016/S0016-7037(99)00204-5

Niespolo, E.M., Rutte, D., Deino, A.L., Renne, P.R. (2017) Intercalibration and age of the Alder Creek sanidine $^{40}Ar/^{39}Ar$ standard. *Quaternary Geochronology* 39, 205–213. https://doi.org/10.1016/j.quageo.2016.09.004

Oliveros, V., Moreno-Yaeger, P. Flores, L. (2020) Igneous Rock Associations 25. Pre-Pliocene Andean Magmatism in Chile. *Geoscience Canada* 47, 65–82. https://doi.org/10.12789/geocanj.2020.47.158

Renne, P.R., Swisher, C.C., Deino, A.L., Karner, D.B., Owens, T.L., DePaolo, D.J. (1998) Intercalibration of standards, absolute ages and uncertainties in $^{40}Ar/^{39}Ar$ dating. *Chemical Geology* 145, 117–152. https://doi.org/10.1016/S0009-2541(97)00159-9

Rochette, P., Gattacceca, J., Devouard, B., Moustard, F., Bezaeva, N.S., Cournède, C., Scaillet, B. (2015) Magnetic properties of tektites and other related impact glasses. *Earth and Planetary Science Letters* 432, 381–390. https://doi.org/10.1016/j.epsl.2015.10.030

van Ginneken, M., Gattacceca, J., Rochette, P., Sonzogni, C., Alexandre, A., Vidal, V., Genge, M. J. (2017) The parent body controls on cosmic spherule texture: Evidence from the oxygen isotopic compositions of large micrometeorites. *Geochimica et Cosmochimica Acta* 212, 196–210. https://doi.org/10.1016/j.gca.2017.05.008